Eur. Phys. J. A **41**, 155–168 (2009)
DOI 10.1140/epja/i2009-10805-7

THE EUROPEAN PHYSICAL JOURNAL A

Regular Article – Experimental Physics

Background study and Monte Carlo simulations for large-mass bolometers

C. Bucci[1], S. Capelli[2,3], M. Carrettoni[2,3], M. Clemenza[2,3], O. Cremonesi[3], L. Gironi[2,3], P. Gorla[1], C. Maiano[2,3], A. Nucciotti[2,3], L. Pattavina[2,3], M. Pavan[2,3,a], M. Pedretti[3,4], S. Pirro[3], E. Previtali[3], and M. Sisti[2,3]

[1] INFN, Laboratori Nazionali del Gran Sasso, I-67010 Assergi (L'Aquila), Italy
[2] Dipartimento di Fisica, Università degli Studi di Milano-Bicocca, I-20126 Milano, Italy
[3] INFN, sezione di Milano Bicocca, I-20126 Milano, Italy
[4] Dipartimento di Fisica e Matematica, Università dell'Insubria, I-22100 Como, Italy

Received: 7 January 2009 / Revised: 20 April 2009
Published online: 10 July 2009 –
Communicated by E. Bellotti

Abstract. Large-mass bolometers are today extensively used for dark matter and double beta decay searches, in both cases the ultimate experimental sensitivity is defined by the background level reached in such devices. The most common background sources and the techniques used for their identification and reduction are here reviewed, with a particular focus on double beta decay searches. The relevant role played by Monte Carlo simulations in this field is discussed. As a real case, the background optimization in the MiDBD experiment is described.

PACS. 29.40.-n Radiation detectors – 23.40.-s β decay; double β decay; electron and muon capture

1 Introduction

The use of cryogenic particle detectors (or bolometers) for particle physics and astronomy was first suggested in the '80s [1] and was followed by a successful technological development. Today micro-bolometers (with masses smaller than few grams) are used in X-ray astronomy and β decay measurements. Macro-bolometers (with masses ranging from few grams to hundreds of grams) are used for *Rare-Event Physics*: double beta decay [2], dark matter [3–5] and rare nuclear decay searches [6,7]. The application of macro-bolometers to rare-event physics is the subject of this paper, in which we will discuss in detail a specific aspect of the bolometer development: background reduction.

The operation of a detector aiming at a search for *rare events* implies the removal of any spurious source that can mimic the *rare event* (*e.g.*, radioactive sources or cosmic rays). The residual background counting rate measures the sensitivity of the experiment [8,9]. As a consequence, one of the main issues of present and future $\beta\beta(0\nu)$ and dark matter experiments is the identification, control and reduction of the radioactive background [10]. This field is rather new and unexplored for bolometers since most of the experimental activity was concentrated so far on their technical development, aiming at the improvement of their resolution and stability as well as at the increase of their mass. We will focus our attention on double beta decay, whereas a similar work for dark matter can be found in [11].

[a] e-mail: pavan@mib.infn.it

2 Background sources

A review of the various sources that generally contribute to the background recorded by a Ge solid-state detector (but identical considerations apply to macro-bolometers and to most solid-state detectors) is contained in the paper by G. Heusser [12] that treats also the different origin of these sources and the techniques for their suppression. Here we limit ourselves to list the most common sources for macro-bolometers:

1. *natural contaminants*, mainly ^{238}U, ^{235}U and ^{232}Th with their radioactive chains and the β/EC decaying ^{40}K isotope;
2. *anthropogenic contaminants*, generally residual of nuclear explosion in the atmosphere, radioactive leakages by nuclear plants and radioactive isotopes used in industrial processes, like ^{60}Co, ^{90}Sr, ^{137}Cs, ^{134}Cs and ^{207}Bi isotopes;
3. *cosmogenic activation*, *i.e.* isotopes produced by cosmic-ray interactions (for example in copper the following isotopes are produced: ^{57}Co, ^{58}Co, ^{60}Co and ^{54}Mn);

4. *environmental background at the experiment location*: cosmic rays, environmental gammas and neutrons.

The first two sources are controlled by accurate material selection and handle. In the special case of ^{222}Rn also the air has to be controlled. This is particularly important in underground sites where radon emissions from the rock can accumulate in air and give rise to particularly large radon concentrations, if compared with the usual atmospheric content above ground.

Cosmogenic activation is controlled by reducing the exposure of materials to cosmic rays and by avoiding —as far as possible— the use of nuclei with large activation cross-section. While for thermal neutron interactions the cross-sections are well known, in the case of high-energy neutrons or protons (as it is for cosmic-ray particles) uncertainties on the activation reactions are larger. Simulation codes, based on theoretical evaluations of the cross-sections, are generally used to predict the rate of activation under cosmic-ray radiation [13,14]. In some special cases dedicated measurements are realized to evidence the presence of any dangerous nuclear activation [15].

In the case of the fourth background source the mandatory requirement for a *rare-event* experiment is to be located underground. Indeed, only a sufficiently large rock overburden can ensure a relevant reduction of the most penetrating component of cosmic rays: muons. In typical underground laboratories the muon flux is reduced by several orders of magnitude, while all the other components of cosmic-ray radiation are negligible and only secondaries (*i.e.* particle produced by muon interaction in the rock) are present. These are neutrons and gamma rays. Also the rock radioactivity is a source of neutrons (through (α, n) and fission reactions). The flux of such neutrons is much more intense than the one of muon-induced neutrons, their spectrum is however softer with an end point at few MeV. Finally, environmental gammas are dominated by rock radioactive emission, having a cut-off at 2.6 MeV: above this energy the flux has a dramatic decrease. Gammas are rather easily shielded with high-Z materials like lead, while neutrons are shielded with hydrogen-rich materials (for thermalization) added with high neutron capture cross-section nuclei. Finally, veto systems are used for the rejection of the background induced by muons interaction in the set-up.

2.1 Material selection

Traditionally, this selection is based on gamma-ray spectroscopy using high-purity germanium (HPGe) detectors, but recently the use of different and more specialized techniques has grown in importance [16–20]. These are mass spectroscopy (one of the most sensitive being the Inductive Coupled Plasma Mass Spectroscopy (ICPMS)), α spectroscopy (employing Si surface barrier detectors) and Neutron Activation Analysis (NAA) (see table 1).

HPGe gamma spectroscopy is by far the most widely used technique, since most radioactive impurities have intense and characteristic gamma emissions. The sensitivity depends on the Ge diode efficiency and on its background level. The achievement of very high sensitivities (μBq/kg) requires high-purity detectors, an underground installation and a dedicated heavily shielded set-up as well as a strict control over any possible external contaminant.

Table 1. Sensitivities (mBq/kg) achieved in copper analysis with different techniques. ^{232}Th and ^{238}U are assumed in secular equilibrium. The quoted sensitivities refer to measures done: at sea level in Milano with a 100% HPGe [19] (I), underground at Laboratori Nazionali del Gran Sasso (LNGS) with a 110% HPGe diode [19] (II), with ICPMS [20] (III), in Milano with a 100% HPGe diode using a sample irradiated at the LENA nuclear reactor in Pavia [19] (IV).

Method	^{232}Th	^{238}U	^{210}Pb	^{60}Co	^{40}K
I (HPGe - Milano)	1	10	–	10	1
II (HPGe - LNGS)	0.01	0.01	10^4	0.01	0.1
III (ICPMS)	0.01	0.04	–	–	–
IV (NAA)	0.003	0.1	–	–	–

ICPMS is a technique for elemental analysis that can be also used for the measurement of radionuclide concentrations. Sensitivities comparable with those achievable with gamma spectroscopy are feasible for long living isotopes.

NAA is a multi-element analytical technique used to identify trace elements in a sample. The technique consists in irradiating the sample with thermal neutrons and later measure the gamma emission of the sample, identifying the metastable isotopes created by neutron capture on the sample impurities. Among the radioactive impurities that can be searched for with NAA there are ^{238}U and ^{232}Th chains. In this case primordial parents of these chains are activated and the gammas emitted by ^{233}Pa (at 311.9 keV) and ^{239}Np (at 106.1 keV and 277.6 keV) are observed.

Finally, Si Surface barrier detectors are used to investigate the presence of α/β radioisotopes in the sample. Due to the short range of α/β particles this technique measures only the radioactive content of the first surface layer of the sample, a layer which is often interested by an excess contamination with respect to the sample bulk. This kind of contamination is particularly dangerous if the detector —like it is for bolometers— does not have a dead layer.

2.2 Shielding and veto

Environmental gammas and cosmic rays are reduced by means of proper shields. The Laboratori Nazionali del Gran Sasso (LNGS), L'Aquila, Italy, where all our bolometric arrays have been operated, have a rock overburden corresponding to a minimum thickness of 3100 mwe. There, environmental emissions are due to the rock radioactivity and to the residual muon flux. In fig. 1 we report the gamma-ray spectrum, as measured by a small Ge diode (the detector is a portable model, a HPGe 59 mm in diameter and 58 mm in height) in the Hall A of LNGS. The gamma-ray flux originating this spectrum was reconstructed (tables 2 and 3) using the JAZZY code,

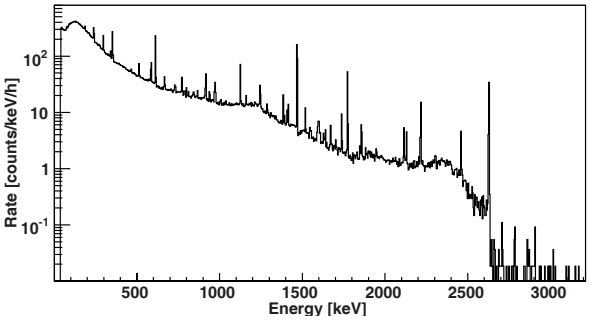

Fig. 1. Gamma-ray spectrum measured at LNGS (Hall A) with a small Ge diode.

Table 2. Intensity of the main gamma lines ($\gamma/m^2/day$) measured in the underground Hall A of LNGS. Only lines with intensity higher than $10^6\,\gamma/m^2/day$ are listed. These are due to ^{40}K, and to the ^{238}U and ^{232}Th chains.

Energy [keV]	Isotope	Intensity [$\gamma/m^2/day$]
238.6	^{212}Pb	$2.8 \cdot 10^6$
295.2	^{214}Pb	$3.8 \cdot 10^6$
352	^{214}Pb	$7.9 \cdot 10^6$
583	^{208}Tl	$3.0 \cdot 10^6$
609	^{214}Bi	$1.3 \cdot 10^7$
911	^{228}Ac	$3.1 \cdot 10^6$
934	^{214}Bi	$2.1 \cdot 10^6$
968	^{228}Ac	$2.1 \cdot 10^6$
1120	^{214}Bi	$6.3 \cdot 10^6$
1238	^{214}Bi	$2.8 \cdot 10^6$
1460	^{40}K	$2.9 \cdot 10^7$
1764	^{214}Bi	$8.2 \cdot 10^6$
2204	^{214}Bi	$3.1 \cdot 10^6$
2614	^{208}Tl	$7.8 \cdot 10^6$

Table 3. Gamma-ray flux ($\gamma/m^2/day$) in the underground Hall A of LNGS. The integral gamma-ray flux below 3 MeV is $\sim 6.3 \cdot 10^8\,\gamma/m^2/day$.

Energy interval [keV]	gamma flux [$\gamma/m^2/day$]
0–500	$4.4 \cdot 10^8$
500–1000	$1.1 \cdot 10^8$
1000–2000	$7.0 \cdot 10^7$
2000–3000	$1.3 \cdot 10^7$

discussed in sect. 4.2. The reconstruction was based on the assumption of an isotropic gamma-ray flux.

In a deep site the neutron flux below ~ 10 MeV (at LNGS this is $\sim 4 \cdot 10^{-6}\,n/s/cm^2$) is mainly due to fission and (α, n) processes in the rock. In both cases it is rock radioactivity that generates neutrons. Neutrons with energies above ~ 10 MeV are produced by muon interaction in the rock, and their flux is generally much lower than the one due to neutrons produced by rock radioactivity. For example at LNGS the neutron flux changes by about 3 orders of magnitude when crossing the 10 MeV neutron energy [21–23]. Simulations for both radioactivity-induced and muon-induced neutrons are found in the literature [24–27]. In the case of radioactivity-induced neutrons the comparison with experimental results is rather good, while in the case of muon-induced neutrons this comparison is not possible since this component dominates the environmental neutron flux only above ~ 10 MeV, a region where poor experimental data are available. Existent simulations for the LNGS mountain yield an integral flux, for muon-induced neutrons, 3 orders of magnitude lower than the radioactivity-induced one [24,27].

Neutrons are absorbed after moderation —using hydrogen-rich compounds (*e.g.*, water and polyethylene)— while absorption is based on high neutron capture cross-section isotopes (B and Li are among the best ones because in the neutron absorption reaction they do not emit gamma rays).

Muons, being deep penetrating particles, cannot be removed by a shield. At LNGS the average muon energy is of 270 GeV with an integrated flux of $\sim 3 \cdot 10^{-6}\,\mu/s/cm^2$, the differential flux and zenith angle dependence have been measured by MACRO [28] and LVD [29]. Generally, it is not muon direct interaction in the detector, but the gamma and neutron background arising from their interaction in the set-up that is particularly dangerous. The presence of heavy, high-Z shields (increasing muon interaction probability) makes the situation even worse. The only way to get rid of this background —in those experiments in which it could be dangerous— is by the use of a muon veto to reject any muon-induced interaction.

3 Bolometers

Cryogenic particle detectors are very sensitive calorimeters which measure the energy deposited by a single interacting particle through the corresponding temperature rise [1]. Unlike other solid-state devices, bolometers are not ionization detectors but phonon detectors. As a consequence they are almost equally sensitive to any kind of particle, despite the way energy is released. In other words electrons, α-particles and nuclear recoils, depositing the same amount of energy in the detector, produce a pulse with the same amplitude (and shape) [30]. This property and the absence of a surface dead layer make the study of background sources in bolometers a little bit different from other, more traditional, detectors.

In the last 15 years our group has operated several TeO_2 bolometric arrays in the two low-temperature refrigerators installed in the underground Hall A (fig. 2) and Hall C of LNGS [2,31–33]. Both the refrigerators are heavily shielded with lead to reduce the impact of environmental radioactivity. They are provided with an external neutron shield and have been built with low-radioactivity materials (mainly copper). In the case of the Hall A cryostat an additional internal Roman lead shield surrounding the detector is usually installed to reduce the effects of the residual cryostat contamination. This material is obtained

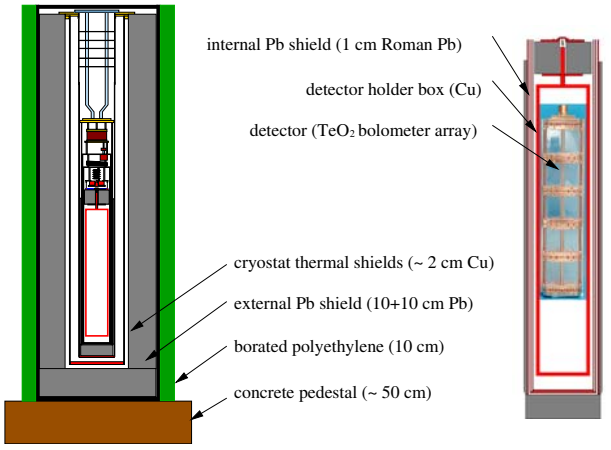

Fig. 2. Left: Hall A set-up. Right: the inner part of the refrigerator with the MiDBD array as in phase 1 configuration.

from the lead bricks found in the wreck of a Roman ship sunk near Sardinia coasts [34]. Its extraordinary low ^{210}Pb content [35] is due to the metallurgical process that separated —about 2000 years ago— the lead from any other chemical impurity, including the isotopes of the ^{238}U chain that are responsible of ^{210}Pb production. In 2000 years the ^{210}Pb —untouched by the metallurgical processes— decayed.

Our arrays were optimized to search for the $\beta\beta(0\nu)$ decay of ^{130}Te, therefore much effort was dedicated over the years to background reduction in the region where the $\beta\beta(0\nu)$ line should appear (2530 keV). This work was accomplished by an accurate selection of low-contamination materials, by the realization and operation of small bolometer prototypes used for test purposes and by the analysis —supported by Monte Carlo simulations— of the measured background.

4 Monte Carlo simulations

Monte Carlo simulations play a primary role in background identification and reduction. First, because the interpretation of HPGe and Si barrier spectroscopy measurements requires Monte Carlo simulation for efficiency evaluation and background interpretation. Second, because the comprehension of the sources responsible of the background measured by an experiment rely on Monte Carlo simulations modelling the experimental apparatus and its possible contamination.

In Milano two different Monte Carlo codes (JAZZY for Si and Ge diodes, TOWER for bolometers arrays) have been used extensively since the beginning of the '90s, to study and improve our background knowledge. Since 2001 both are based on GEANT-4 [36]. All the results discussed in this paper have been obtained with GEANT 4.8.2 version, using the LBE (Low Background Experiment) physics list. In the next sections a brief description of the two simulation codes is given. For both the codes the decay scheme generation is provided by the GENDEC package and the simulated detector output by G2TAS.

4.1 Event generation: GENDEC

This package has been developed by our group in the '90s, to correctly simulate chains of radioactive decays in secular equilibrium, in order to obtain useful information for contamination inside the detectors and to fully exploit the capability of detector arrays in terms of coincidence analysis.

Starting from *ad hoc* written input files for the nuclear and atomic structures, the package provides the simulation codes with the sequence of all particles emitted following one decay of the first nuclide in the chain. The sequence contains the type of particle, its energy and the time delay with respect to the previous one. The package with its input files can manage alpha, beta (β^-, β^+ and electron capture EC) and gamma decays. Various $\beta\beta$ modes are also considered. In the case of α decays the recoiling nucleus is included in the sequence. Gamma decays include the possibility of the internal conversion IC up to the shell N. EC can happen to the K, $L1$ and $L2$ shells.

In the case of both EC and IC, the atomic relaxation radiation is included in the sequence. The vacancies created in the K, $L1$, $L2$ and $L3$ shells are recursively shifted to the upper shells by both radiative (X-rays) and non-radiative (Auger and Coster-Kronig) transitions. When the vacancy reaches the M or higher shells, the whole available energy is assigned to a single electron. A total of up to 14 radiative transitions and 14 non-radiative transitions are possible.

We have compiled the input files by critically selecting the data available in the literature. The nuclear-structure files contain the information concerning the nuclear levels with their energies and lifetimes, and the transitions between the levels with their branching ratios. In addition they may contain the pertinent parameters for the EC and IC probabilities and for the type of β decay (*i.e.* the degree of forbiddeness). For each nuclide, data has been taken from the most recent Nuclear Data Sheet compilation for the corresponding A multiplet or directly from the appropriate Evaluated Nuclear Structure Data File (ENSDF) [37]. For the IC coefficients, experimental data from those two sources have been used whenever possible. Missing or incomplete data have been integrated by logarithmic interpolation of tables in [38–40]. The same has been done for the EC probabilities from the different shells: missing data have been integrated using [41]. The β decay spectra are generated including all corrections for the screening of the nuclear Coulomb field by atomic electrons (Fermi factor) and for the energy dependence of the matrix element for the given decay degree of forbiddeness.

The atomic-structure files contain the binding energies, the radiative transition energies and intensities, the yields for the various non-radiative processes, and the intensities of the Auger transitions (their energies are calculated starting from the binding energies [42]). The atomic data are taken from the appendices in [42] and used following the methods described therein.

As a benchmark both the experimental data in the Nuclear Data Sheets (or in the ENSDF) and the evaluated data in [42] have been used: the files have been filled with

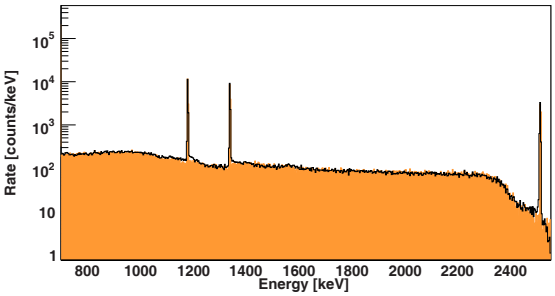

Fig. 3. A HPGe source measurement obtained with a certified ^{60}Co source. The experimental spectrum (black line) is compared with the JAZZY simulation (filled histogram). The simulation is normalized on the basis of the certified activity of the source.

all the levels and transitions required to reproduce all the gamma, X-ray and electron lines listed with an absolute intensity higher than 0.1%.

As an example, the nuclear-structure input file for the ^{232}Th natural chain contains 83 nuclear levels and 240 transitions (alpha, beta and gamma). With this input file, the particle generated by GENDEC with an absolute intensity larger than 0.05% are: about 150 gammas, about 150 X-rays, about 550 electrons (atomic or IC) and 19 alphas, plus, of course, the electrons emitted in the β decays.

The individual nuclide files can be easily combined to generate broken chains in secular equilibrium. The GENDEC package does not include the Inner Bremsstrahlung radiation and any kind of angular correlation between decays.

GENDEC has been distributed publicly in the past. Today also GEANT provides the user with a similar package. We still use GENDEC both for historical reason and because GENDEC uses decay data that have been accurately cross-cheked.

4.2 JAZZY

JAZZY is a multipurpose code that allows to model HPGe and Si surface barrier detectors having different geometries. The geometric features of the detector and of the source (the sample to be measured) are defined through an external macro. The Ge diodes description is based on the constructor data sheets that is later checked (investigating the real sensitive volume) by accurate calibration measurements performed with certified gamma sources. Each part of the detector and of the sample is considered by the simulation as an independent element that can be made active (*i.e.* a contamination within its volume or on its surface can be simulated). An element is identified by its geometrical shape and material composition.

Figure 3 shows a comparison of simulation and data in the case of a certified ^{60}Co source. The absolute activity of the source, as extrapolated from the experimental data using the efficiency evaluated for the 1173 and 1332 keV gamma lines of ^{60}Co, is in quite good agreement with the known activity of the source (the simulation overestimates the line activities by about 7%). As clearly seen from the figure also the sum line of the two gammas (at 2505 keV), as well as the continuum are correctly reproduced.

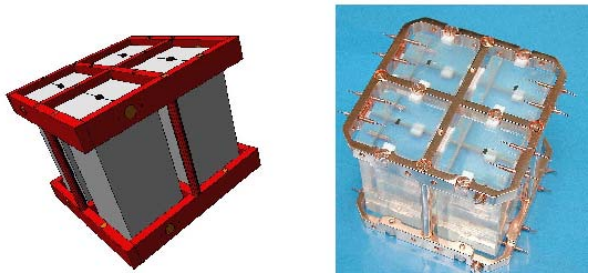

Fig. 4. MiDBD I geometry in TOWER compared with the true geometry. The four crystal plane (picture on the right) and its simulated geometry (plot on the left) are shown.

4.3 TOWER

TOWER is the code used for the simulation of bolometric arrays. It models in detail the shields and the cryostat of the experimental set-ups installed in Hall A and Hall C at LNGS. The geometries of the MiDBD [32] array (in the 2 different configurations), of CUORICINO [2], as well as that of the small arrays used for radioactivity tests in Hall C, are all taken into account in the same code. Elements in this simulation are the crystals, the copper structure that holds the array, the germanium sensors glued on the crystals, their gold connecting wires, the silicon resistors, the PTFE spacers, the various copper vessels and lead shields that surround the array. Each of them can be studied as an active source whose bulk or surface contamination can be simulated independently. In the case of surface contaminants the depth of the contaminated layer and the density profile of the contaminant can be defined by the user.

TOWER includes the propagation of photons, electrons, α-particles and heavy ions (nuclear recoils from α emission), as well as neutrons and muons. Figure 4 shows a comparison of simulated and true geometry in the case of the MiDBD array.

4.4 Detector simulated outputs: G2TAS

The output of the Monte Carlo simulation contains the following information: event number, detector number, time, energy and kind of particle. An external code G2TAS allows then to produce the simulated detector outputs (spectra and *n*tuple). G2TAS takes into account the features of the detector response and of the data analysis procedure in order to ensure a comprehensive reproduction of the experimental conditions. This includes the reproduction of the detector energy resolution and of its variation with energy, the introduction of a programmable detector threshold (events below threshold do not contribute to spectra and are not used for tagging a coincidence),

the computation of causal (within the decay chain) or casual (rate dependent) pile-up events and the computation of coincidence signals. In particular:

- an *integration* time can be specified in which two interactions depositing energy in the same detector are considered as a single event, having an energy equal to the sum of the energies deposited in the two interactions;
- a *rate* for the source can be specified in order to generate casual and not only causal coincidences and pile-ups;
- a *pile-up* time for the rejection of multiple events can be introduced. In this case two or more events occurring in the same detector, with a time separation greater than the integration time but below the pile-up time, are rejected. Such a special feature is important for bolometers since they are quite slow detectors (TeO_2 bolometers as those used in MiDBD and CUORICINO have typical decay times of the order of hundreds of ms) and are intrinsically paralyzable (*i.e.* the energy of the pulse occurring on the tail of a precedent one cannot be correctly evaluated);
- in the case of array of detectors, *coincidence* patterns can be invoked when computing spectra and scatter plots, as it is for experimental data.

5 Modelling background in bolometric arrays

In this section we discuss the background analysis for a bolometric array experiment. We show how the use of close-packed arrays not only has the advantage of significant background suppression, thanks to the anticoincidence cuts, but also allows to collect quite useful information on the background source nature and location through the study of the multi-hit events. Indeed, by cross-checking dedicated and independent contamination measurements (with the techniques described in sect. 2) with Monte Carlo simulations of the experimental apparatus it is possible to model the background sources and to make predictions for future experiments with a rather good accuracy. As an example of a successful application of this technique we report the results obtained in the study of the background sources of the MiDBD experiment.

In modelling background in our detectors we strongly focused our attention on two energy regions: the region centered at 2530 keV where the ^{130}Te neutrinoless decay should appear ($\beta\beta(0\nu)$ region in the following) and the region just above the 2615 keV ^{208}Tl line (the 3–4 MeV region). As discussed later, these two regions —being very near to each other— are both affected by the same kind of background, namely the one produced by degraded α-particles coming from the radioactive chains of ^{238}U and ^{232}Th. However, a relevant feature differentiates the two regions: the 3–4 MeV is nearly unaffected by gamma radioactivity while the $\beta\beta(0\nu)$ region is often dominated by the ^{208}Tl gamma activity. As a consequence one can look at the 3–4 MeV region to measure contributions that in the $\beta\beta(0\nu)$ region are *covered* by the ^{208}Tl gamma activity.

Table 4. FWHM resolutions in a calibration spectrum and in the 84000 *hours* × *detector* sum background spectrum of the MiDBD experiment. The resolution on the α line is obtained fitting the right side of the ^{238}U line at 4238 keV. This line is visible only in the sum background spectrum and it is ascribed to a surface contamination of the crystals. The left side of this peak has a tail due to alphas that lose a fraction of their energy outside the crystal, for this reason only the left side of the peak is used to evaluate the detector resolution in the α region.

Line energy [keV]	583	911	1764	2615	4238
FWHM [keV] calibr.	3.6	4.3	5.9	8.1	–
FWHM [keV] backgr.	4.2	5.1	6.7	9.3	25

5.1 Data collected with a bolometric array

The most relevant features and results obtained with TeO_2 bolometer arrays can be found in [2,31–33]. In all cases an almost similar hardware (detector structure, electronics and DAQ) has been employed: data were collected operating each crystal as a completely independent particle detector, provided with its own read-out chain, trigger and DAQ system. The voltage signal, amplified and filtered, is fed into a 16-bit ADC. For each triggered signal the entire waveform, a sample of 512 or 1024 points (~ 4 s long), was saved to disk for off-line analysis. This included pulse shape analysis (rejection of spurious triggers) and gain instability corrections [43]. A periodic calibration of the detectors was obtained with an exposure to a ^{232}Th source. The gamma lines used for calibration ranged from 511 and 2615 keV. The non-linear behavior of the detectors was corrected by linearization of the energy spectra with a proper fit function whose extrapolation was used to calibrate the spectra above 2615 keV. Once corrected, the spectra of the different detectors were added as if collected with the same device.

As an example of the typically achieved results, the FWHM energy resolution in a calibration *sum* spectrum ($\sim$ 3 days) and that in the background *sum* spectrum (various months) in the MiDBD experiment are reported in table 4 (*sum* spectra are obtained by adding together the energy-calibrated spectra of all the detectors). Lacking calibration measurements for the α region, we have to rely on the use of an extrapolation of the gamma conversion, which —above 3 MeV— results in spectra of the single detector that are affected by systematic and different, among each other, calibration errors. As a consequence, when summed together, the α peaks of the different detectors are spread out and the resolution of the array as a whole results worsened with respect to the average resolution of the single detector in the α region [44]. The same happens to the single detector when different runs are summed, each provided with its own gamma calibration.

Different typologies of spectra are produced by the off-line analysis, according to the selected coincidence pattern. Multi-hit events (in which more detectors in the array trigger) can be studied to investigate background sources, while cuts rejecting such events (keeping only the

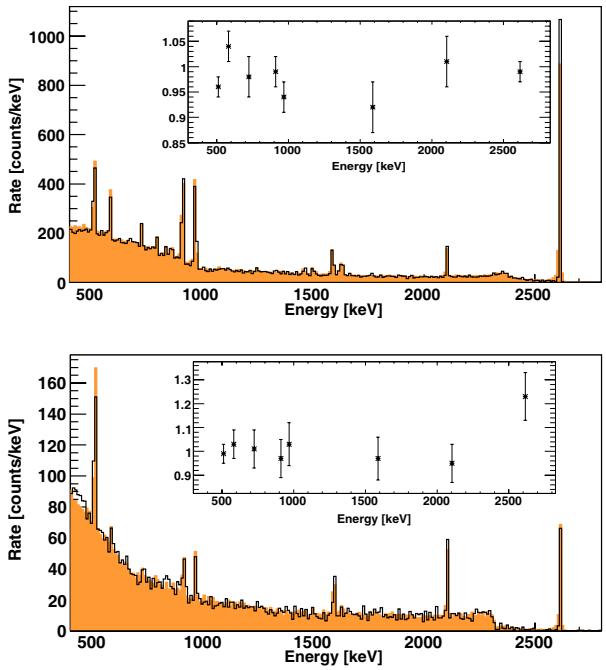

Fig. 5. A calibration measurement obtained by exposing a TeO_2 bolometric array to a ^{232}Th source. The measured spectrum (filled histogram) is compared with the TOWER simulation (black-line histogram). Top panel: the single-hit (anticoincidence) spectra. Bottom panel: the double-hit (coincidence) spectra. In the two graphical inserts the ratios between simulated and measured intensity for the main gamma peaks are shown.

single-hit type) can be applied to reduce the background for DBD analysis. For MiDBD TeO_2 crystals the probability that both the electrons emitted in $\beta\beta(0\nu)$ decay are stopped inside the same crystal where the decay took place is 84%. This efficiency was evaluated simulating ^{130}Te $\beta\beta(0\nu)$ decays (with the correct energy distribution for the two electrons kinetic energy) with TOWER.

5.2 Validation of the simulation

Figure 5 shows a comparison between the simulated and measured spectra of a ^{232}Th source in the MiDBD bolometric array. The sources used for calibration are two thoriated wires introduced in the gap between the cryostat and the external lead shield, on two opposite sides of the array. The normalization factor between simulated and measured spectra is obtained as the ratio of the number of counts in the 500–2500 keV interval in the single-hit spectra (this same normalization factor is used for double-hit spectra). Lines and continuum are reproduced at better than 5%, both in the single-hit and in the double-hit sum spectra (as shown in the two inserts in fig. 5).

5.3 Background model and analysis procedure

The background sources considered in our analysis are those listed in sect. 2. The contaminants are usually considered uniformly distributed in the bulk of the construction materials. Indeed, only in the case of the crystals and of the materials directly facing them it is worth to distinguish between bulk and surface contamination, as they result in different spectral shapes due to the contribution of electrons and alphas. As a first step, the background coming from external neutrons, muons and gammas are considered. These are sources that we know to exist and whose intensity is obtained —in most cases— from direct measurements. Therefore one can simply proceed to the evaluation of their effects on our detectors.

5.3.1 Environmental background

The neutron flux measured at LNGS [21–23] and the high energy fraction of it —as modelled by [25,27]— was simulated through TOWER on our apparatuses resulting in an almost negligible contribution to the experimental background counting rates (see table 5). Moreover, according to the simulations the environmental neutron background does not dominate the background counting rates measured by our detectors, even in the absence of the neutron shield. A cross-check of this result was provided by the comparison of measurements collected before and after the installation of the neutron shield surrounding each of our two cryostats. For example in the case of the MiDBD experiment (Hall A) the background spectra collected before and after the installation of the neutron shield are compatible within the statistical error (*i.e.* they are compatible within 10% in both the $\beta\beta(0\nu)$ and 3–4 MeV regions where the fractional contribution of neutrons should be higher due to the reduced number of sources contributing to background). A similar experimental result was recently obtained in measurements carried out in Hall C. In both cases, the measurements could not achieve a sensitivity good enough to check simulation results. They only helped to verify that the background rates presently measured in our apparatuses are not dominated by neutron background, in agreement with the simulations.

In a similar way, the effect of the muon interaction in our apparatuses was studied, simulating with TOWER the muon fluxes reported by [28,29]. The result shows that muon contribution, although negligible in MiDBD, can be worrisome for next-generation experiments, like CUORE [45], that aims at counting rate in the 2–4 MeV region below 10^{-2} counts/keV/kg/yr. However in bolometer arrays, the anticoincidence cut allows a dramatic reduction of the muon-induced counting rate: in a single tower like MiDBD the reduction factor is more than one order of magnitude.

Finally, also the environmental gamma activity, as resulted by our measurements (fig. 1 and table 2), was simulated resulting in a sizable but not dominating contribution to the background recorded by MiDBD in the region between 500 keV and 3 MeV. Such a contribution, clearly too high for next-generation experiments, can be reduced by means of a thicker lead shield surrounding the set-up.

In conclusion, external sources have quite a minor role in background production. The most likely source of

Table 5. Environmental muon, neutron and gamma counting rates (counts/keV/kg/yr) as predicted by TOWER for a TeO_2 bolometric array working at LNGS (Hall A set-up) compared with the rates measured in MiDBD phase 1. No anticoincidence here is applied. When only single-hit (anticoincidence) events are considered (as usual in $\beta\beta(0\nu)$ and dark matter searches) the background coming from environmental muon and neutron is reduced by more than one order of magnitude. The reduction factor is much lower in the case of environmental gammas.

Energy region	10–50 keV	0.5–1 MeV	1–2 MeV	2–3 MeV	3–4 MeV	4–6 MeV
neutrons	$< 2 \cdot 10^{-4}$	$3 \cdot 10^{-5}$	$(7 \pm 3) \cdot 10^{-6}$	$< 8 \cdot 10^{-6}$	$< 8 \cdot 10^{-6}$	$< 4 \cdot 10^{-6}$
muons	0.14	0.13	$5 \cdot 10^{-2}$	$2 \cdot 10^{-2}$	$1.5 \cdot 10^{-2}$	$1 \cdot 10^{-2}$
gammas	4 ± 2	3.0 ± 0.5	0.9 ± 0.2	0.10 ± 0.03	–	–
MiDBD phase 1	$1.4 \cdot 10^3$	30.2 ± 0.2	6.7 ± 0.1	1.3 ± 0.1	1.2 ± 0.1	8.1 ± 0.3

Table 6. Bulk contamination levels of the materials used in the Hall A set-up. Pb-o and Pb-i refer to the outer and inner 10 cm thick layers of lead used to externally shield the cryostat, Pb-r is the Roman lead used for the shield directly surrounding the detectors. Cu is the copper used for the detector holder parts. TeO_2 refers to the powder used to grow the crystals. Contaminations are in mBq/kg as measured by HPGe spectroscopy (for Roman lead the ^{210}Pb content was measured bolometrically [35]). In parenthesis 90% upper limits, obtained by comparing the MiDBD phase 2 counting rate with Monte Carlo simulations for the different bulk contaminants, are reported.

contaminant	^{232}Th		^{238}U		^{210}Pb		^{60}Co		^{40}K	
Pb-o	< 0.3		< 0.3		$110 \cdot 10^3$		–		–	
Pb-i	< 0.2		< 0.2		$(16 \pm 4) \cdot 10^3$		< 0.5		< 2	
Pb-r	< 0.07	(0.05)	< 0.04	(0.04)	< 4		< 0.2		< 0.5	(0.7)
Cu	< 0.5	(0.06)	< 0.6	(0.07)	–	(170)	< 0.2	(0.2)	< 10	(2)
TeO_2	< 0.8	(0.003)	< 2	(0.002)	–	(0.02)	–	(0.04)	< 100	(0.4)

background in our experiments (like MiDBD and CUORICINO) being the radioactive contaminations of the experimental set-up (shielding, cryostat and detector), as discussed in the next paragraphs.

5.3.2 Background from material contamination

The general method used to identify and localize these background sources is the following: for each element introduced in the simulation and for each contaminant a spectrum is generated.

In the case of a surface contamination different depths and density profiles are considered. U and Th chains are always considered in secular equilibrium except for the case of surface contamination, when breaks of secular equilibrium produce distinguishable and relevant patterns in the α spectrum. Indeed, although manufactured materials are rarely in secular equilibrium, there are only few cases in which the γ spectrum is affected by a break in the decay chain. Since the typical time required for the construction and operation of an experiment is few months, and since only gamma lines with branching ratios above 1% are visible in our measurements, the only case in which a break in secular equilibrium would yield a different pattern in the γ spectrum is in correspondence of the ^{228}Th isotope (1.9 year half-life). However, the comparison of the activities recorded for the 238 keV (^{212}Pb) and the 337 keV (^{228}Ac) lines (where variation in efficiency are small) can be used as an indicator of violation of secular equilibrium. In the case of the analysis presented in the next section such a violation appears to be negligible (see table 7).

Each simulation is then compared with the experimental spectrum and the maximum contamination level compatible with it is determined.

In this way conservative upper limits for impurities concentrations in the different materials are computed (see, for example, table 6 for the results obtained in the MiDBD experiment). These limits are often lower than, or comparable with, those obtained with HPGe spectroscopy.

Finally, the best linear combination that reproduces the measured background (accounting for both continuum and peaks) for coincidence and anticoincidence spectra, as well as scatter plots, is searched for. This is done minimizing the differences among the experimental spectrum and the linear combination of all the simulated spectra.

Available upper limits on impurities levels coming from independent measurements of material contamination (*e.g.*, HPGe spectroscopy) are included in the minimization procedure.

As a first step only the sources responsible for the background above 2.6 MeV are considered. Indeed, a limited number of sources can contribute to the background in this region: once neutrons and muons are excluded, and assuming negligible gamma and β contributions coming from the natural radioactive chains (^{214}Bi β decays with B.R. 0.19% and end point of 3.2 MeV and few very rare gamma-gamma and gamma-beta coincidences), only α-particles (and partially electrons) from the radioactive natural chains have enough energy to produce counts in this region. Moreover, the short range of α-particles allows to restrict the analysis to the crystals and to the materials directly facing them. These are all the detector com-

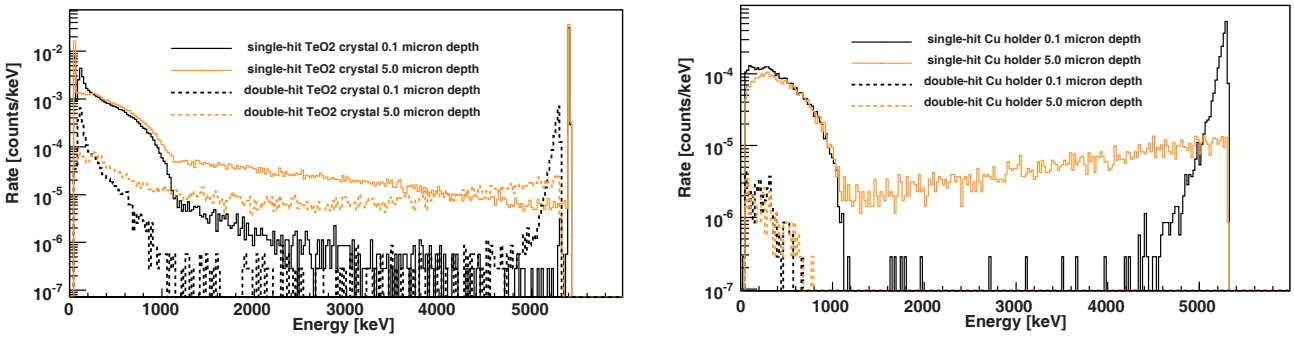

Fig. 6. Simulation of a ^{210}Pb surface contamination with an exponential density profile and a λ of 0.1 μm (black line) and 5.0 μm (colored (on-line) line). The simulation refers to an array of TeO_2 bolometers in which the crystals face for 50% of their surface another crystal and for the other 50% some inert material (mainly the copper of the copper holder). Left: the contamination is on crystal surface. Right: the contamination is on the Cu holder. The dotted lines correspond to double-hit spectra.

ponents: the NTD thermistors, the Si resistors, the glue, the PTFE parts, and finally —and more likely because of its biggest mass and surface— the copper holder. The position and shape of the α peaks as well as the comparison of single-hit and multi-hit spectra allow to distinguish between internal and external, surface or bulk, α contaminations. How this can be done is clearly understood by considering the results of Monte Carlo simulations.

In fig. 6 the different effects of surface contamination on crystals and surrounding elements are shown for a bolometric array (like MiDBD) where about 50% of the crystal surface faces another bolometer while the remaining 50% faces an inert material (the whole in vacuum). The simulated contamination is ^{210}Pb. This isotope β decays to ^{210}Po, that then α decays with a Q value of 5407 keV emitting an α-particle with energy $E_\alpha = 5304$ keV (the daughter nucleus recoils with a kinetic energy of 103 keV). When the contamination is on the crystal surface, as in the left panel of fig. 6, the α line is visible at the transition energy (with an additional broad peak at E_α in the case of very thin contamination). When the contamination is on an inert surface facing the crystal, as in the right panel of fig. 6, the α line is visible, at E_α, only for very thin contaminated layers. As soon as the thickness increases, the spectrum becomes flat. Alpha peaks shape and position are not the only features that allow to distinguish between crystal and surrounding elements contaminations. Indeed, when the contamination is on the crystal surface in a fraction of decays the α (or with lower probability the nuclear recoil) escapes the source crystal and enters the facing one. In this case the two detectors record a coincidence event whose total energy yields the Q value of the α transition. When the energies of coincidence events are tracked, crystal surface contamination gives rise to straight lines with -1 slope, as is shown in fig. 7. Summarizing, in the α region the crystal surface/bulk contamination can be distinctly identified on the basis of quite clear signatures (peak position, peak shape and scatter plots of coincidence events). Moreover, also thickness and density profile can be investigated, given their different signature (fig. 8). More difficult is the identification of contamination of surrounding elements since when deep enough they just produce a flat continuum.

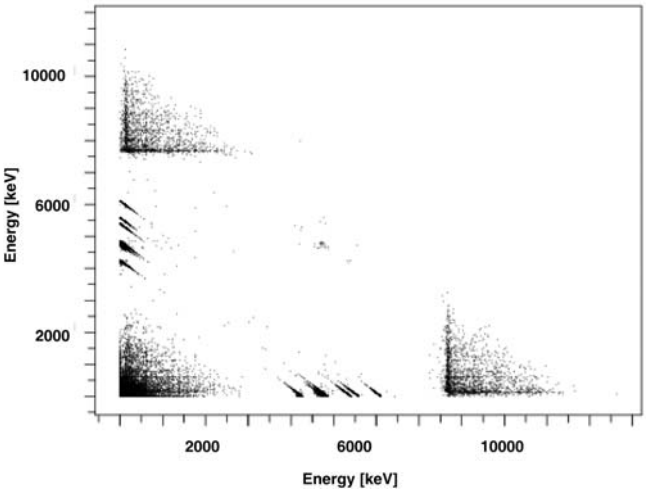

Fig. 7. Scatter plot of double-hit (coincidence) events in the case of a ^{238}U contamination on the bolometer surface (1 μm depth, exponential density profile). The plot refers to a Monte Carlo simulation of a TeO_2 bolometric array where 50% of bolometer surface faces other bolometers.

After having analyzed the region above 2.6 MeV, most of the near sources are identified. These sources generally give a weak contribution (through degraded alphas but also through their gamma emission) to the background below 2.6 MeV. Here the γ emissions from heavy materials outside the detector (*e.g.*, the Roman lead shield, the cryostat elements and the external lead shield) are the main responsible of detector counting rates. The exact localization of the sources is, in this case, much more difficult and the CPU time needed for the simulations increases with the amount of material interposed between the detector and the simulated element. At the same time the simulated spectra become less characteristic and therefore indistinguishable from each other.

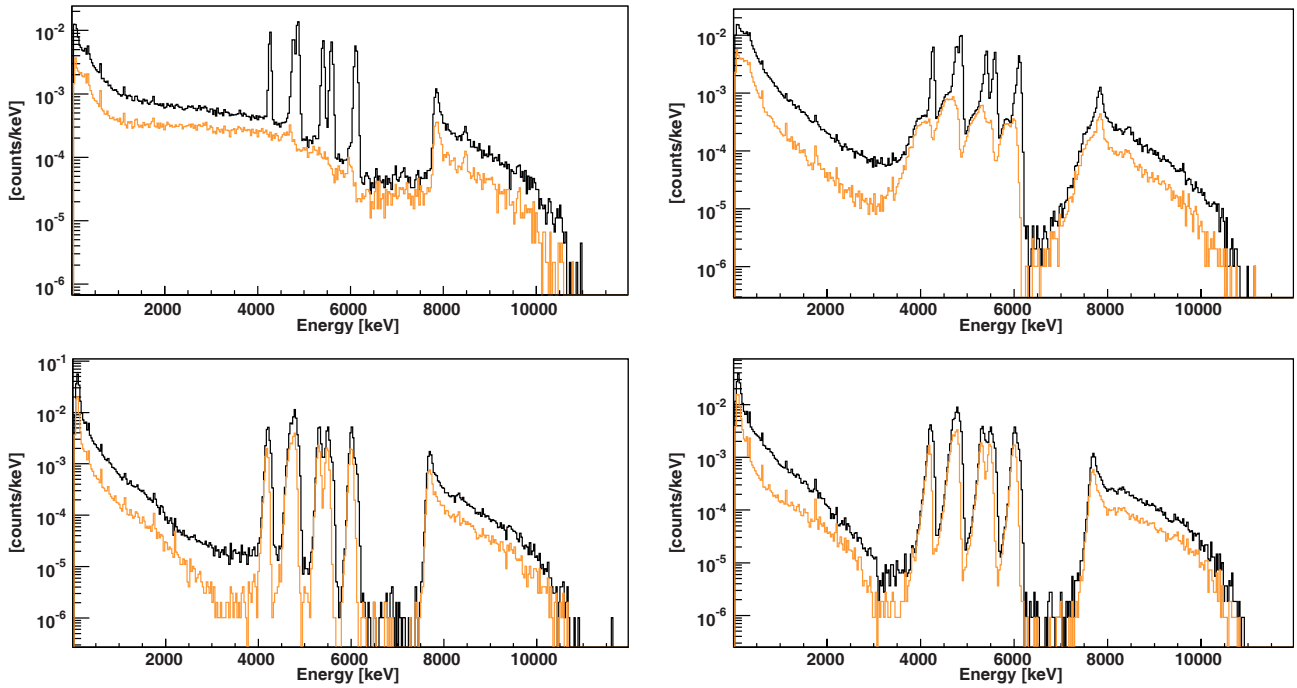

Fig. 8. Simulation spectra produced by a ^{238}U contamination on bolometer surfaces: the black histograms refer to all the events, the colored (on-line) histograms to double-hit (coincidence) events. The top left and right are, respectively, 10 and 0.1 μm depth contamination with a flat density profile. The bottom left and right histograms refer to 1 μm depth contamination with a flat (left) and exponential (right) density profile. The plots refer to a Monte Carlo simulation of a TeO_2 bolometric array where 50% of each bolometer surface faces other bolometers. The lines above 3 MeV are due to the alpha decay of the ^{238}U isotopes. From left to right: ^{238}U, ^{230}Th + ^{226}Ra + ^{234}U, ^{210}Pb, ^{222}Rn, ^{218}Po, ^{214}Po (this line is summed to the ^{214}Bi β decay).

The whole analysis is generally done on sum background spectra since the statistics on single-detector spectra is too low.

6 Understanding the MiDBD experiment

Located in Hall A of LNGS, MiDBD consisted of an array of 20 crystals of TeO_2 of $3 \times 3 \times 6\,cm^3$ (340 g) each, for a total mass of 6.8 kg. The main goal of the experiment was the study of neutrinoless and two neutrino $\beta\beta$ of ^{130}Te to ^{130}Xe. Its results on detector performances and background were the base on which CUORICINO and CUORE experiments were designed. In particular, as we will discuss later, in the construction of the CUORICINO detector the information gained by the Monte Carlo simulations of the MiDBD array were widely —and successfully— exploited.

A description of the experimental set-up is found in [32]. The cryostat (mainly made of copper) is externally shielded with two layers of lead of 10 cm each having different ^{210}Pb content. The array was held in a copper holder inside the inner vacuum chamber (IVC) at about 10 mK. All the materials used for the set-up construction (the lead, the copper used for the thermal shield and for the array holder, the TeO_2) were measured to determine their contamination levels (see table 6). Two different configurations for the detector were used during the experiment:

1. *in phase 1* the array was made by 20 TeO_2 crystals tightly held in a copper box by means of two PTFE masks. The array was surrounded by a 1 cm lateral thickness of Roman lead and a top and bottom lead plates of 10 cm thickness;
2. *in phase 2* the same crystals were re-assembled in a new, more compact, copper structure; reducing the amount of PTFE used to hold the crystals and adding a further layer of Roman lead (2 cm on the side and 5 cm on the top). In this occasion all the surfaces of the TeO_2 crystals and of the Cu mounting structure were subject to an *ad hoc* surface polishing process aiming at the reduction of radioactive contaminants. Phase 2 was intended to test the new mounting system of the crystals and to reduce surface radioactivity that, according to the our analysis, was an important contribution to the $\beta\beta(0\nu)$ background counting rate. An external neutron shield (10 cm of 5% borated polyethylene) was added at the end of this phase for an experimental evaluation of neutron contribution (as discussed in sect. 5.3).

The gamma lines visible in the background spectra of phase 1 and phase 2 are reported in table 7.

6.1 MiDBD phase 1

The large statistics collected during MiDBD phase I allowed a detailed analysis of background sources. This was done —following the technique described in sect. 5.3.2— starting from the region above 2.6 MeV. Here the α peaks

Table 7. Intensity of the main gamma lines (counts/hours) measured in the sum background spectrum of phase 1 (columns 3 and 4) and in phase 2 (columns 5 and 6).

Energy [keV]	Isotope	Rate [counts/h]	Error [counts/h]	Rate [counts/h]	Error [counts/h]
88	^{123m}Te + ^{127m}Te			0.191	0.008
105	^{129m}Te			0.038	0.003
122	^{57}Co	0.002	0.001	0.009	0.002
145	^{125m}Te	0.004	0.001	0.193	0.008
238	^{212}Pb	0.007	0.001		
241	^{214}Pb	0.0019	0.0006		
247	^{123m}Te			0.082	0.006
294	^{214}Pb	0.0032	0.0007	0.025	0.003
337	^{228}Ac	0.0017	0.0006		
351	^{214}Pb	0.0049	0.0009		
511		0.0076	0.0007	0.006	0.002
568	^{207}Bi	0.0060	0.0006	< 0.004	
583	^{208}Tl	0.0046	0.0005	< 0.004	
603	^{121m}Te + ^{121}Te	0.0013	0.0004	0.011	0.002
609	^{214}Bi	0.0031	0.0005		
662	^{137}Cs	0.0032	0.0006		
811	^{58}Co			0.011	0.002
835	^{54}Mn	0.0010	0.0003	0.006	0.002
911	^{228}Ac	0.0047	0.0004	< 0.002	
968	^{228}Ac	0.0023	0.0003	< 0.003	
1060	^{207}Bi	0.0065	0.0005	< 0.003	
1120	^{214}Bi	0.0015	0.0003	< 0.002	
1173	^{60}Co	0.0083	0.0005	0.005	0.002
1332	^{60}Co	0.0075	0.0006	0.004	0.001
1460	^{40}K	0.033	0.001	0.006	0.002
1764	^{214}Bi	0.0020	0.0003	< 0.001	
2104	^{208}Tl (single escape)	0.0009	0.0002	0.0013	0.0007
2203	^{214}Bi	0.0006	0.0002		
2615	^{208}Tl	0.0051	0.0005	0.0017	0.0007

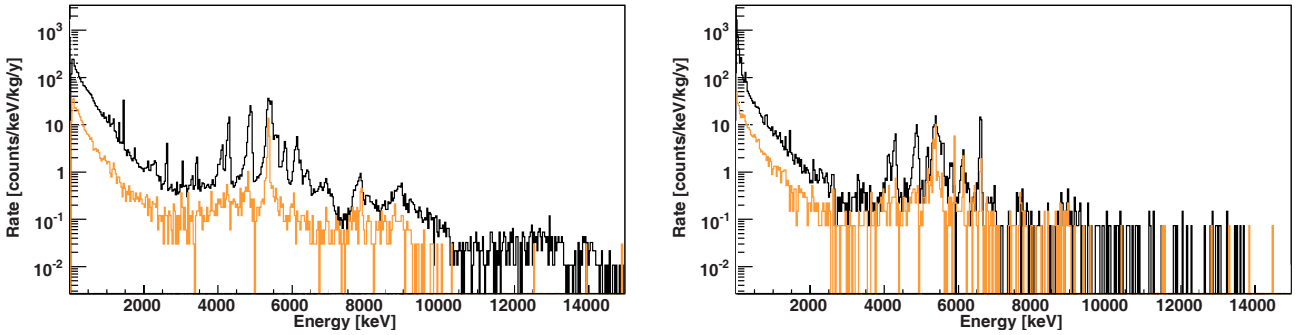

Fig. 9. Anticoincidence (black line) and coincidence (colored (on-line) line) sum background spectra of MiDBD crystals. Left: phase 1. Right: phase 2.

clearly visible in fig. 9 show the presence of a ^{238}U and ^{232}Th contamination of the crystals. The peak energy position corresponds to the transition energies of the decay implying that both the α-particle and the nuclear recoil contribute to the signal: the decaying nuclei can only be *contained* in the crystal. Moreover, the coincidence spectra indicate that the contamination producing the peaks is localized on the crystals surface. The low-energy tail of the peaks is then explained in terms of the fraction of the decays occurring very near to the surface, where part of the α or of the recoil energy or —when it is the case— the gamma ray emitted in the decay is lost outside the crystal. When plotting coincident events in different faced detectors the characteristic scatter plot of

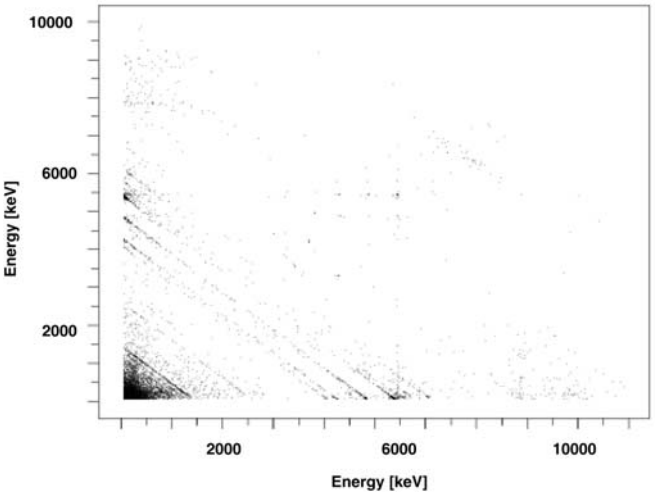

Fig. 10. Scatter plot of coincident events on facing crystals in MiDBD phase 1.

surface contamination is obtained (fig. 10). The analysis of double-hit events not only yields a further proof that α peaks are due to a surface contamination of the crystals, but also proves that this contamination produces a continuous background extending far below the α decay transition energy. In particular this source can partially —but not completely— account for the rather flat continuous background measured between 3 and 4 MeV by all our arrays, a region where neither γ nor α lines from natural and cosmogenic radioactivity are usually present.

Two peaks visible in fig. 9 (and similarly in the spectra of most of our devices) are not ascribed to surfaces: the one at ~ 3.3 MeV due to ^{209}Pt and the other at ~ 5.3 MeV due to ^{210}Po. The former peak is ascribed to crystal inclusions of small amounts of Pt due to residuals of the crucible in which TeO_2 crystals are grown. ^{209}Pt has a natural isotopic abundance of 0.001%, decays with a half-life of $6.5 \cdot 10^{11}$ years emitting an α of 3.249 MeV.

The latter can only be explained by an extremely thin surface contamination of ^{210}Pb on the inert material facing the crystals. Indeed, as shown in fig. 6, when the α source is outside the detector its contribution is visible (at E_α) only when distributed on a very thin and shallow layer, while thicker contamination produce just a flat background.

Below 2.6 MeV additional contribution to background coming from the set-up elements has to be considered. We have grouped the various parts of the set-up in four elements whose radioactive contamination in ^{238}U and ^{232}Th produces characteristic and distinguishable spectra:

- the material inside the Roman lead shield (mainly the copper of the detector coverage);
- the Roman lead shield;
- the cryostat (modelled only by its thermal shields, a series of copper cylinders that constitute the heaviest part of the entire refrigerator);
- the external lead shield.

The comparison of measured and simulated spectra, and the use of the information we have on the contamination of most of these elements (for the Hall A set-up these contaminations are reported in table 6) allow to localize most of the background sources.

The background composition, as obtained from our analysis, for MiDBD phase 1 is the following:

- TeO_2 *bulk contamination*: just limits of the order of 10^{-12} g/g for ^{238}U, ^{232}Th and ^{40}K. A ^{210}Po and a ^{190}Pt contamination;
- TeO_2 *crystal surface contamination*: a ~ 0.1 micron deep contamination of about $0.05\,\mu$Bq/cm^2 in ^{238}U, a contamination in ^{232}Th lower by one order of magnitude, and finally a very thin (< 0.001 micron depth) contamination in ^{210}Pb (most likely due to Rn);
- *array copper holder*: a $\sim$ 10 micron deep contamination of about $0.2\,\mu$Bq/cm^2 if in ^{238}U and ^{232}Th or of $\sim 3\,\mu$Bq/cm^2 if in ^{210}Pb (our data do not allow to disentangle the separate contribution of the three radioisotopes and their chains) and a very thin (< 0.001 micron deep) contamination in ^{210}Pb (most likely due to Rn). A ^{60}Co bulk contamination ascribed to neutron activation;
- *internal Roman lead shield*: no relevant contributions from ^{238}U and ^{232}Th;
- *cryostat thermal shield and superinsulation*: the most likely source for the ^{238}U and ^{232}Th lines;
- *external lead shield*: contributes to background through the Bremsstrahlung of ^{210}Pb and its 803 keV gamma line; no relevant contribution from ^{238}U and ^{232}Th contaminations;
- *environmental gammas*: an integral contribution lower than 5% to the integral rate.

A ^{40}K and a ^{210}Pb contamination, not precisely localized (due to their weak signature) have to be added to this list. These two contributions are indeed needed to justify the continuous background in both anticoincidence and coincidence spectra.

In this analysis only surface contaminations having an exponential density profile have been used, since these appear to fit better to our experimental spectra. The error in the identification of the contamination depth is of about a factor 2.

Finally, it has to be noted that what we call *array copper holder* includes all the small parts directly in contact with the detector: PTFE elements, wires, pins an so on. Since the copper holder is by far the largest mass in that region and since we have rather stringent limits on the small parts contamination, it is natural to ascribe the *near source* identified in our analysis to the copper holder. A combination of more than one contribution from small parts and copper holder cannot be, however, excluded. Figure 11 displays the comparison between experimental and simulated background.

The most relevant result coming from this analysis was the evaluation of the background sources responsible for the counting rate in the $\beta\beta(0\nu)$ region. We obtained (43 ± 13)% from TeO_2 surface contamination in ^{232}Th and ^{238}U, (23 ± 11)% from the surface contamination of

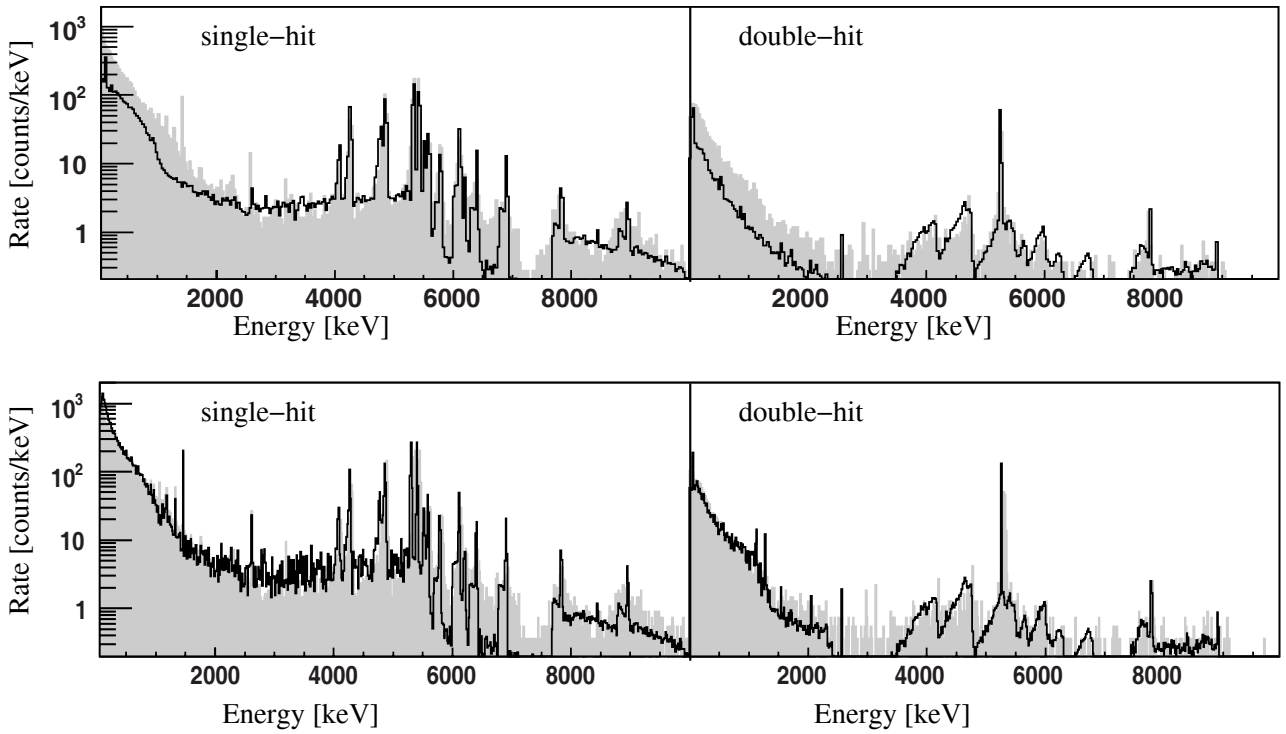

Fig. 11. Background reconstruction in MiDBD phase 1. MC simulations (black line) are compared with experimental results (gray-filled histograms). Both single-hit (left) and (double-hit) spectra are shown. In the upper plots only contributions from ^{238}U, ^{232}Th, ^{210}Pb and ^{190}Pt contamination of TeO_2 crystals and mounting structure are considered. In the lower plots contribution from sources outside the detector as well as from isotopes like ^{60}Co and ^{40}K are also considered.

the holder, $(20 \pm 5)\%$ from the Compton events due to the 2615 keV ^{208}Tl line ascribed to the thermal shields and/or the superinsulation contamination in ^{232}Th.

6.2 MiDBD phase 2

Starting from the results of the above analysis, and of complementary information that came from independent measurements performed in Hall C with small size TeO_2 arrays, a surface treatment procedure was applied to all the crystals of MiDBD aiming at the reduction of their surface contamination. Also the surface of the copper holder was treated with mechanical and chemical procedures. A thicker internal Pb shield was added just outside the detector holder. On the basis of the expected reduction of the α surface contamination (tests in Hall C proved that we were able to reach at least a factor-2 reduction) and of the expected reduction of the ^{208}Tl contribution due to the thicker lead shield (in our model ^{208}Tl came from outside the lead shield) we expected a background reduction in the $\beta\beta(0\nu)$ region by about a factor 2.

Indeed, MiDBD phase-2 results showed a sizable reduction (a factor 2 in intensity) of the α peaks as well as a reduction of the overall counting rate (table 8). In the $\beta\beta(0\nu)$ region the reduction factor was estimated to be 1.5 ± 0.3 in fairly good agreement with what we extrapolated by our model.

Table 8. Background reduction factors measured between the two runs of MiDBD. The $\beta\beta(0\nu)$ region is centered at ^{130}Te transition energy (2530 keV) with a width of about 50 keV.

Reduction factors: γ and α peaks			
U and Th γ's	^{60}Co γ's	^{40}K γ's	U and Th α's
≥ 2	~ 2	~ 6	~ 2
Reduction factors: continuum			
[1–2] MeV	[2–3] MeV	$\beta\beta(0\nu)$ region	[3–4] MeV
~ 1.3	~ 1.6	1.5 ± 0.3	~ 2.4

Due to the much lower statistics collected during this phase it was not possible to perform a completely independent analysis of the data to extract contamination values.

7 Conclusion

The use of Monte Carlo simulations to reproduce the experimentally measured background is a powerful tool often used to identify and localize background sources. Careful checks of the simulation capability of reproducing the detector geometry, as well as the detector behavior, are obviously necessary to verify the reliability of the model.

The use of independent information on background sources, such as measurements of environmental fluxes (cosmic rays, gammas and neutrons) and material con-

tamination levels, is also mandatory to constrain free parameters.

We have shown that whenever these requirements are satisfied a reliable reconstruction of background is possible. In particular in the case of bolometric arrays the *segmentation* of the detector provides by itself a powerful tool to cross-check simulation results with experimental data. Indeed, requiring the reproduction of the background spectrum recorded by the detector as a whole, as well as that of the coincidence patterns among the various elements of the array, strongly constrain the *parameter phase space*.

References

1. N. Booth, B. Cabrera, E. Fiorini, Annu. Rev. Nucl. Part. Sci. **46**, 471 (1996); C. Enss, D. McCammon, J. Low Temp. Phys. **151**, 5 (2008).
2. C. Arnaboldi *et al.*, Phys. Rev. Lett. **95**, 14501 (2005).
3. D.S. Akerib *et al.*, Phys. Rev. Lett. **93**, 211301 (2004).
4. A. Benoit *et al.*, Phys. Lett. B **545**, 43 (2002).
5. G. Angloher *et al.*, Astropart. Phys. **18**, 1 (2002).
6. A. Alessandrello *et al.*, Phys. Rev. C **67**, 014323 (2003).
7. Marcillac *et al.*, Nature **422**, 876 (2003).
8. V.I. Tretyak, Yu.G. Zdesenko, At. Data Nucl. Data Tables **80**, 83 (2002); S. Elliott, P. Vogel, Annu. Rev. Nucl. Part. Sci. **52**, 115 (2002); A. Morales, J. Morales, Nucl. Phys. B (Proc. Suppl.) **114**, 141 (2003); O. Cremonesi, Nucl. Phys. B (Proc. Suppl.) **118**, 287 (2003); K. Zuber, Acta Pol. B **37**, 1905 (2006); F.T. Avignone III, S.R. Elliott, J. Engel, arXiv:hep-ph/0708.1033 (2006).
9. M.W. Goodman, E. Witten, Phys. Rev. D **31**, 3059 (1985); J.D. Lewin, P.F. Smith, Astropart. Phys. **6**, 87 (1996); J.D. Vergados, J. Phys. G **22**, 253 (1996).
10. C. Dorr, H.V. Klapdor-Kleingrothaus, Nucl. Instrum. Methods A **513**, 596 (2003); H. Gomez *et al.*, Astropart. Phys. **28**, 435 (2007).
11. S. Fiorucci *et al.*, Astropart. Phys. **28**, 143 (2007).
12. G. Heusser, Annu. Rev. Nucl. Part. C **45**, 543 (1995).
13. R. Silberberg, C.H. Tsao, Astrophys. J. **501**, 911 (1998).
14. J. Martoff, P.D. Lewin, Comput. Phys. Commun. **72**, 96 (1992).
15. H. Miley *et al.*, Nucl. Phys. B (Proc. Suppl.) **28A**, 212 (1992); F.T. Avignone *et al.*, Nucl. Phys. B (Proc. Suppl.) **28A**, 280 (1992); S. Cebrian *et al.*, J. Phys. Conf. Ser. **39**, 344 (2006).
16. *Proceedings of the 2nd Topical Workshop on Low Radioactivity Techniques, LTR 2006*, AIP Conf. Proc., Vol. **897** (2007).
17. M. Laubenstein *et al.*, Appl. Rad. Isotopes **61**, 167 (2004).
18. D. Budjas *et al.*, Appl. Rad. Isotopes **67**, 755 (2009).
19. S. Capelli, CUORE Internal Notes CUORE-2008-01, `http://crio.mib.infn.it`.
20. D.S. Leonard *et al.*, Nucl. Instrum. Methods A **591**, 490 (2008).
21. P. Belli *et al.*, Nuovo Cimento A **101**, 959 (1989).
22. F. Arneodo *et al.*, Nuovo Cimento **112**, 819 (1999).
23. M. Cribier *et al.*, Astropart. Phys. **4**, 23 (1995).
24. H. Wulandari *et al.*, *Neutron flux at the Gran Sasso Underground Laboratory Revisited*, hep-ex/0312050.
25. H. Wulandari *et al.*, *Neutron Background Studies for the CRESST Dark Matter Experiment*, hep-ex/0401032.
26. M.J. Carson *et al.*, *Simulation of neutron background in a time projection chamber relevant to dark matter searches*, hep-ex/0503017.
27. D.M. Mei, A. Hime, Phys. Rev. D **73**, 053004 (2006).
28. M. Ambrosio *et al.*, Phys. Rev. D **52**, 3793 (1995); M. Ambrosio *et al.*, Astropart. Phys. **19**, 313 (2003).
29. A. Dementyev *et al.*, Nulc. Phys. B (Proc. Suppl.) **70**, 486 (1999); A. Dementyev *et al.*, Nucl. Instrum. Methods A **314**, 380 (1992).
30. A. Alessandrello *et al.*, Nucl. Instrum. Methods A **409**, 451 (1998).
31. A. Alessandrello *et al.*, Phys. Lett. B **285**, 176 (1992); A. Alessandrello *et al.*, Phys. Lett. B **335**, 519 (1994).
32. C. Arnaboldi *et al.*, Phys. Lett. B **557**, 167 (2003).
33. CUORE Collaboration, LNGS Annual Report 2005 and LNGS Annual Report 2006, `www.lngs.infn.it`.
34. A. Alessandrello *et al.*, Nucl. Instrum. Methods B **61**, 106 (1991).
35. A. Alessandrello *et al.*, Nucl. Instrum. Methods A **142**, 454 (1998).
36. S. Agostinelli *et al.*, Nucl. Instrum. Methods A **506**, 250 (2003); J. Allison, IEEE Trans. Nucl. Sci. **53**, 270 (2006); GEANT4, `http://geant4.web.cern.ch/geant4`.
37. `http://www.nndc.bnl.gov/ensdf/`.
38. F. Rösel, H.M. Fries, K. Alder, At. Data Nucl. Data Tables **21**, issues nos. 2, 3, 4, 5 (1978).
39. I.M. Band, M.B. Trzhaskovskaya, M.A. Listengarten, At. Data Nucl. Data Tables **21**, 1 (1978).
40. I.M. Band, M.B. Trzhaskovskaya, At. Data Nucl. Data Tables **55**, 43 (1993).
41. W. Bambynek *et al.*, Rev. Mod. Phys. **49**, issue no. 1 (1977).
42. E. Browne, R.B. Firestone, *Table of Radioactive Isotopes*, edited by V.S. Shirley (Wiley-Interscience, John Wiley & Sons, Inc, New York 1986).
43. A. Alessandrello *et al.*, Nucl. Instrum. Methods A **412**, 451 (1998).
44. A. Alessandrello *et al.*, Nucl. Instrum. Methods A **440**, 397 (2000).
45. C. Arnaboldi *et al.*, Astropart. Phys. **20**, 91 (2003); C. Arnaboldi *et al.*, Nucl. Instrum. Methods A **518**, 775 (2004).